

Electronic and Excitonic Properties of Semi-Hydrogenated Borophene Sheets

Mohammad Ali Mohebpour,¹ Shobair Mohammadi Mozvashi,¹ Sahar Izadi Vishkayi,² and Meysam Bagheri Tagani^{1,*}

¹*Computational Nanophysics Laboratory (CNL), Department of Physics,
University of Guilan, P. O. Box 41335-1914, Rasht, Iran.*

²*School of Physics, Institute for Research in Fundamental Sciences (IPM), P. O. Box 19395-5531, Tehran, Iran.*

Borophene has triggered a surge of interest due to its outstanding properties including mechanical flexibility, polymorphism, and opto-electrical anisotropy. Very recently, a novel semi-hydrogenated borophene, called α' -4H, was synthesized in large-scale freestanding samples, which exhibits excellent air-stability and semiconducting nature. Herein, using the density functional theory (DFT) and many-body perturbation theory (MBPT), we investigate the electronic and excitonic optical properties of α' -4H borophene. The DFT results reveal that by breaking the mirror symmetry and increasing the buckling height of pure α' borophene, hydrogenation causes an orbital hybridization and opens an indirect band gap of 1.49 eV in α' -4H borophene. This value is corrected to be 1.98, 2.23, and 2.52 eV under the G_0W_0 , GW_0 , and GW levels of theory, respectively. The optical spectrum achieved from solving the Bethe-Salpeter equation shows an optical band gap of ~ 2.40 eV, which corresponds to a strongly bound and stable bright exciton with a binding energy of ~ 1.18 eV. More importantly, the excitonic states are robust against tension up to 10%, where the monolayer is dynamically stable. We also design and study the bilayer α' -4H borophene with different stackings. For the weak van der Waals interactions between the layers, the bilayer can preserve most of the structural and electronic properties of the monolayer. Our study exposes the underlying physics behind the structural, electronic, and optical properties of α' -4H borophene and suggests it as a very promising candidate for flexible optoelectronic applications.

I. INTRODUCTION

Two-dimensional (2D) boron, also known as borophene, is recently considered as a game-changing player of future electronics because of its exceptional properties including polymorphism, electronic and optical anisotropy, ultrahigh thermal conductance, optical transparency, and phonon-mediated superconductivity.¹⁻⁶ Moreover, short B-B bonds and low atomic mass leads to very outstanding mechanical characteristics in borophene.⁷ Numerous studies have studied the applications of borophene in rechargeable ion batteries, gas storages, catalysts, and sensors.^{8,9} Several recent studies have focused on the use of borophene in flexible electronics, wearable devices, and medicines, owing to its flexible nature, low mass density, and non-toxicity.^{10,11}

Boron has three valence electrons and, to compensate its octet completion deficiency, it tends to make highly-delocalized multicenter bonds, resulting in a vast structural diversity and polymorphism.¹² Several motifs of borophene have been proposed and synthesized up to now, among which are α , α' , β , and χ phases, which have trigonal structures with different numbers and positions of hexagon holes (HHs).^{13,14} Different phases of borophene are defined in terms of parameter $\nu = n/N$, where n and N are the numbers of HHs and boron atoms in a unit cell, respectively. Most of the physical properties of borophenes strongly depend on this morphology variable, thus, there is a wide set of options to reach a borophene phase with desired properties. Furthermore, unlike other 2D materials, borophene undergoes a structural phase transition, rather than direct fracturing under tensile strain.⁷

Due to its atomic arrangement, borophene cannot be exfoliated mechanically. Therefore, other methods such as chemical vapor deposition, molecular beam epitaxy, and liquid phase exfoliation should be used.¹⁵ Moreover, because

of its electron deficiency, borophene cannot be stable in a free-standing form and support of a metal substrate is required.¹⁶ Several successful syntheses have been reported on Ag, Cu, Ni, and Au substrates.¹⁷⁻¹⁹ It is worth mentioning that the Ag, Cu, and Ni substrates donate electrons to, and Au substrate withdraws electrons from borophene, hence, the borophenes grow flat on the former substrates and buckled on the latter one.^{7,20}

Because of its high reactivity, most of boron nanostructures suffer from rapid oxidation and presence of other ambient contaminations.⁷ Surface modification is found to be a capable tool for enhancing the stability and electronic properties of nanostructures.^{21,22} Specifically, hydrogenation is reported widely to have a major impact on the stability of borophene and other two-dimensional materials.^{23,24}

Recently, Hou et al¹⁰ have prepared a novel semi-hydrogenated borophene phase in large quantities by in-situ decomposition of NaBH_4 under the exposure of hydrogen. This borophene was named α' -4H because it is similar to α' borophene, with 4 adsorbed hydrogen atoms in each unit cell. The α' -4H borophene has three major advantages which make it very attractive. First, it has high dynamical stability in freestanding form: by withdrawing electrons from the boron atoms, hydrogenation acts similar to an Au substrate, resulting a stable buckled structure. Second, it is stable in the air for a long time: the screening of hydrogen passivates the surface of borophene and prevents it from reactions with oxygen or other ambient atoms. Third, unlike other phases, α' -4H borophene has an energy band gap of ~ 2.5 eV, which brings hopes for its applications in optoelectronics as a semiconductor.

One of the most important drivers of recent advances in condensed matter physics is the feedback Ping-Pong between theory and experiment. High-quality theoretical and computational investigations can truly guide the experiments towards novel materials with desired properties. Moreover,

discussing the underlying physics of quantum systems improves the physical insights and enhances the theory for future advances. To have a small contribution to this trend, in our previous work, we systematically investigated the mechanical flexibility and strength of α' -4H borophene by first-principle calculations.²⁵ We also demonstrated dynamical stability, mechanical anisotropy, high strain compliance, and tunable band gap for this monolayer.

In this paper, we investigate the electronic and excitonic optical properties of α' -4H borophene using ab-initio many-body calculations. By density functional theory (DFT) calculations, we initially discuss the microscopic aspects in which the metallic α' borophene turns into the semiconducting α' -4H. We show how hydrogenation leads to an orbital hybridization and opens a wide band gap of 1.49 eV at the PBE level of theory.

Many-body effects (electron-electron and electron-hole interactions) are significantly enhanced in low-dimensional systems.^{26,27} This is mainly due to the reduced Coulomb screening and geometrical confinement. Hence, we expect to see the critical influence of electron-electron and electron-hole interactions on the electronic and optical properties of α' -4H borophene. First, we calculate the quasiparticle band gap to be 1.98, 2.23, and 2.52 eV at the G_0W_0 , GW_0 , and GW levels of many-body calculations, respectively. Then, we solve the Bethe-Salpeter equation on top of quasiparticle energies (the so-called GW+BSE) to obtain the optical spectrum. It shows that the direct optical excitation is characterized by an optical band gap of ~ 2.40 eV, which corresponds to a strongly bound and stable Frenkel exciton with a binding energy of ~ 1.18 eV, making α' -4H borophene a desirable candidate for exploring optical applications.

Finally, we design and investigate the bilayer α' -4H borophene with different stackings and discuss that for the weak van der Waals interaction between the layers, the bilayer can preserve most of structural and electronic properties of the monolayer and can be used for similar applications. Our results bring insights about physical properties of the monolayer and bilayer α' -4H borophene and suggest it as a promising material for flexible optoelectronic applications.

II. THEORETICAL BACKGROUND

We start the density functional theory (DFT) calculation to find the ground-state eigenvalues (E_{nk}) and eigenfunctions (Φ_{nk}) by solving the Kohn-Sham equation given below:

$$(T + V_{n-e} + V_H + V_{xc})\Phi_{nk} = E_{nk}\Phi_{nk}, \quad (1)$$

where T is the kinetic energy operator, V_{n-e} the Coulomb potential of the nuclei, V_H the Hartree potential, and V_{xc} the exchange-correlation potential. The quasiparticle (QP) energies (E_{nk}^{QP}) are determined within the GW approximation as a first-order perturbative correction to the DFT single-

particle energies (E_{nk}).^{28,29}

$$E_{nk}^{QP,1} = Re[\langle \Phi_{nk} | T + V_{n-e} + V_H + \Sigma_{xc}(G, W; E_{nk}) | \Phi_{nk} \rangle] = E_{nk} + \langle \Phi_{nk} | \Sigma^{GW} - V_{xc} | \Phi_{nk} \rangle, \quad (2)$$

where $\Sigma = iG_0W_0$ is the self-energy operator. This equation is solved non-self-consistently. Therefore, it is the simplest level of theory (the so-called G_0W_0) and computationally the most efficient one. It calculates the QP energies from a single iteration by neglecting all off-diagonal elements of the self-energy and employing a Taylor expansion of the self-energy around the DFT energies. The noninteracting Green's function (G_0) is directly calculated from single-particle orbitals and energies as:

$$G_0(r, r', \omega) = \sum \frac{\Phi_{nk}(r)\Phi_{nk}^*(r')}{\omega - E_{nk} - i\eta \operatorname{sgn}(E_F - E_{nk})}, \quad (3)$$

where E_F is the Fermi energy and η a positive infinitesimal quantity. The noninteracting screened Coulomb potential (W_0) is obtained by the inverse dielectric function (ϵ^{-1}) and bare Coulomb interaction (v) as below:³⁰

$$W_0(r, r', \omega') = \int dr'' \epsilon^{-1}(r, r'', \omega') v(r'', r'). \quad (4)$$

At higher levels of theory (i.e. G_iW_0 and G_iW_i), the updated QP energies ($E_{nk}^{QP,i+1}$) are achieved from the QP energies of the previous iteration as follows:

$$E_{nk}^{QP,i+1} = E_{nk}^{QP,i} + Z_{nk} Re[\langle \Phi_{nk} | T + V_{n-e} + V_H + \Sigma_{xc}(G, W; E_{nk}) | \Phi_{nk} \rangle - E_{nk}^{QP,i}], \quad (5)$$

where the renormalization factor (Z_{nk}) is given by:³¹⁻³³

$$Z_{nk} = (1 - Re \langle \Phi_{nk} | \frac{\partial}{\partial \omega} \Sigma(\omega) |_{E_{nk}^{QP,i}} | \Phi_{nk} \rangle)^{-1}. \quad (6)$$

At the GW_0 level of theory, the Green's function (G) is iteratively updated while the screened Coulomb potential (W) is kept fixed at the initial DFT value. At the GW level, both of them are reevaluated at each iteration (i). Here, the exact (interacting) Green's function is linked to its non-interacting version with the Dyson equation given as, $G = G_0 + G_0 \Sigma G$.³⁴

The imaginary part of the macroscopic dielectric function is obtained by summation over the empty conduction bands within the long-wavelength limit ($q \rightarrow 0$).³⁵

$$Im \epsilon_{\alpha\beta}(\omega) = \frac{4\pi^2 e^2}{\Omega} \lim_{q \rightarrow 0} \frac{1}{|q|^2} \sum_{c,v,k} 2w_k \delta(\epsilon_{ck} - \epsilon_{vk} - \omega) \times \langle u_{ck+e_{\alpha}q} | u_{vk} \rangle \langle u_{ck+e_{\beta}q} | u_{vk} \rangle^*, \quad (7)$$

where q is the Bloch vector of the incident wave, w_k the k -point weight, Ω the volume of the unit cell, and u_{ck} the cell periodic part of the wave function. The vectors e_α are unit vectors for the three Cartesian directions. The indices c and v correspond to the conduction and valence band states, respectively. The electron-hole excited states are characterized by the expansion:³⁶

$$|S\rangle = \sum_c \sum_v \sum_k^{elec\ hole} A_{cvk}^S |cvk\rangle, \quad (8)$$

where A^S is the amplitude of a free electron-hole pair configuration composed of the electron state $|ck\rangle$ and the hole state $|vk\rangle$. It is achieved from the diagonalization of the following excitonic equation:^{37,38}

$$(E_{ck}^{QP} - E_{vk}^{QP})A_{cvk}^S + \sum_{c'v'k'} \langle cvk | \Xi^{e-h} | c'v'k' \rangle A_{c'v'k'}^S = \Omega^S A_{cvk}^S, \quad (9)$$

where E_{ck}^{QP} (E_{vk}^{QP}) denotes the QP eigenvalues of valance (conduction) band at a specific k -point, kernel Ξ^{e-h} describes the screened interaction between excited electrons and holes, and Ω^S is the excitation energy.

III. COMPUTATIONAL DETAILS

The first-principles calculations were performed in the framework of DFT, using the generalized gradient approximation developed by Perdew-Burke-Ernzerhof (GGA-PBE) and the projector augmented waves (PAW) pseudopotentials implemented in the Quantum ESPRESSO package.³⁹ The energy cutoff for the plane-wave basis set was set to be 60 Ry. The Brillouin zone was integrated with a $13 \times 13 \times 1$ Γ -centered k -point mesh. The atomic positions and lattice parameters were fully relaxed until a force convergence of 10^{-3} eV/Å was achieved. A vacuum space of $L_z = 20$ Å was considered to avoid spurious interactions.

The many-body perturbation calculations were carried out using the GW approximation. The eigenvalues and eigenstates achieved from DFT-PBE served as input to calculate the QP energies. The calculations were performed under different levels of self-consistency including single-shot (i.e. G_0W_0) and partially self-consistent (i.e. GW_0 and GW). A compromised set of input parameters (e.g. $9 \times 9 \times 1$ k -point mesh, $L_z = 25$ Å, 40 virtual bands, and 4 iterations) was utilized for our GW calculations.

The QP band structure was interpolated at the G_0W_0 level using the maximally localized Wannier functions (MLWFs) implemented in the WANNIER90 code.⁴⁰ Here, the sp^3 and s orbitals of B and H atoms were respectively chosen for the initial projections. The excitonic optical properties were investigated by solving the Bethe-Salpeter equation (BSE) on top of GW eigenvalues and wave functions, using the Tamm-Dancoff approximation (TDA). This approximation takes only

the resonant part of the BS Hamiltonian into account. The 10 highest valence bands and the 10 lowest conduction bands were considered as the basis for the excitonic eigenstates.

IV. RESULTS AND DISCUSSION

A. Structural and electronic properties

The structural configurations of fully relaxed α' and α' -4H borophenes are displayed in FIG. 1 (a, b) and the corresponding structural parameters are listed in Table S1. As can be seen, the pure α' borophene is nearly flat ($\Delta = 0.37$ Å) and isotropic, with a hexagon hole concentration of $\nu = 1/8$. The hydrogenation leads to an increase in the buckling in α' -4H borophene ($\Delta = 0.88$ Å), owing to the attraction between B and H atoms. The lattice constants of the two monolayers are similar (5.05 Å) but the isotropy of the lattice breaks after hydrogenation. As a result, the bond length increases from isotropic 1.68 Å to anisotropic 1.69 and 1.77 Å.

FIG. 1 (a, b) also indicate the electron density cut planes of α' and α' -4H borophenes. In α' borophene, we can see a “sea of electrons”, which is apparently the cause of its metallic nature. However, in α' -4H borophene, an electron accumulation takes place around H atoms, which lowers the in-plane carrier distribution and decreases the electronic conductivity.

As mentioned above, the α' -4H borophene was synthesized recently.¹⁰ To validate our model with the experiment, we performed simulations of Raman spectrum and scanning tunneling microscopy (STM). FIG. 1 (c) represents the calculated Raman spectrum of α' -4H borophene. We can see three peaks at about 700, 1100, and 2200 cm^{-1} . The first two peaks are representatives of E_g and $A_{1g} + E_g$ modes of the B-B cluster, and the last peak is associated with the combined modes of the B-H bonds. We also indicated the simulated STM image of α' -4H borophene in FIG. 1 (d), which is very similar to the experimentally obtained image. Our calculated Raman spectrum and simulated STM image support the experimental data very well,¹⁰ therefore, we can assure that our simulated model is completely similar to the synthesized α' -4H borophene.

FIG. 2 summarizes the structural and electronic properties of α' and α' -4H borophenes. As shown in the inset of FIG. 2 (a, b), the atomic sites in α' borophene are classified into 6- and 5-bonded boron atoms, labeled with ① and ②, respectively. There are two ① and six ② sites in each unit cell and we can see both inversion and mirror symmetry in α' borophene. After hydrogenation, four ② sites break a B-B bond and make a B-H bond instead, which leads to novel sites labeled with ③. As a result, hydrogenation breaks the mirror symmetry and only preserves the inversion symmetry in α' -4H borophene. These changes directly affect the electronic states and should be considered as one of the origins of different properties in the two borophenes.

FIG. 2 also represents the partial density of states (PDOS)

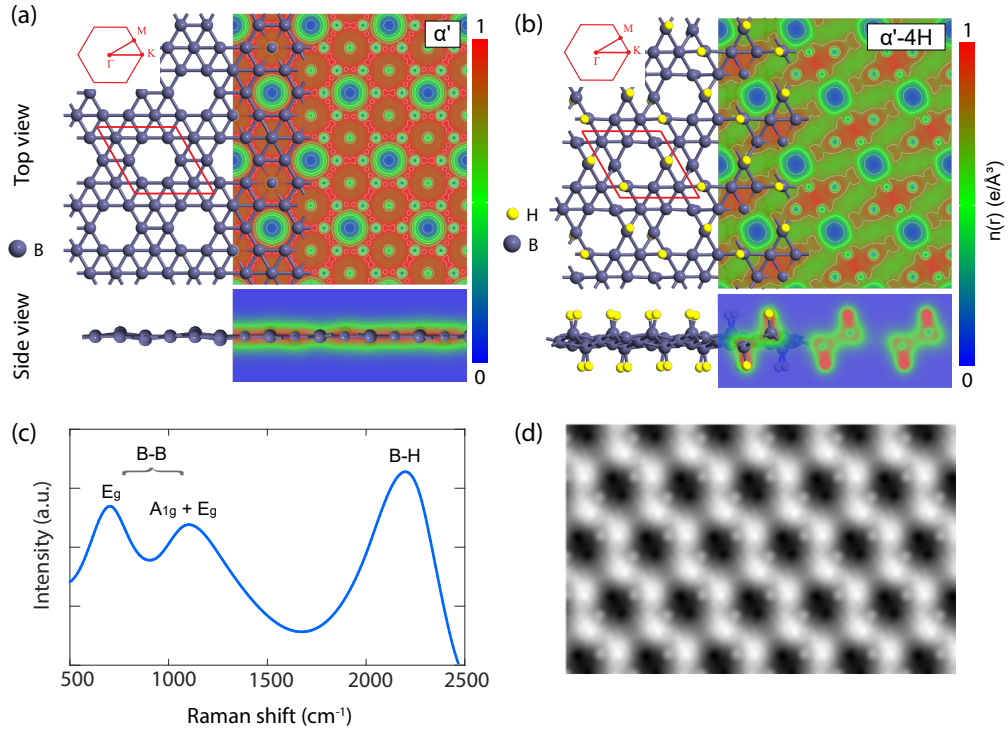


FIG. 1. **(a, b)** Structural configurations and electron density cut planes of α' and α' -4H borophenes. **(c)** Simulated Raman spectrum and **(d)** simulated STM image of α' -4H borophene.

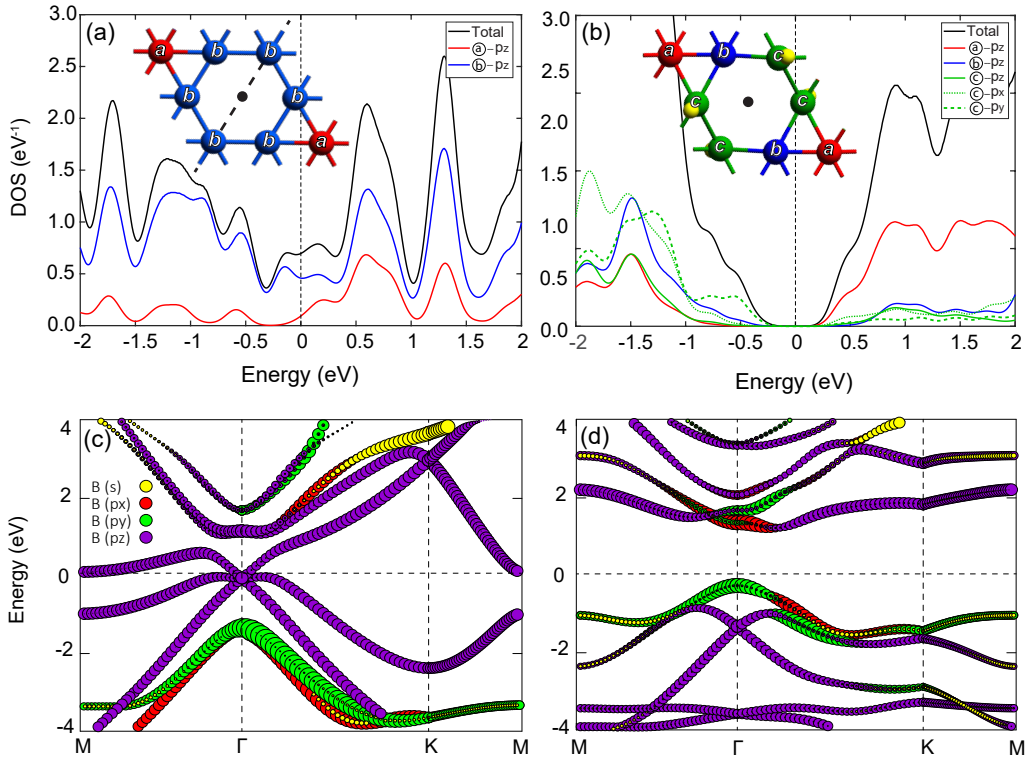


FIG. 2. **(a, b)** Partial density of states (PDOS) of α' and α' -4H borophenes, showing the significant contributing orbitals of the labeled atomic sites shown in the insets. Full results of PDOS are also available in FIG. S1. **(c, d)** Orbital decomposed band structures of α' and α' -4H borophenes. Both PDOS and band structure were calculated at the GGA-PBE level of theory.

and orbital decomposed band structures of α' and α' -4H borophenes at the GGA-PBE level. This information gives valuable insights into the contribution of each atomic site and orbital in the electronic properties. As it is clear, in α' borophene (left panel), p_z orbitals of the \textcircled{b} sites are dominant. Given that α' borophene is almost flat, p_z orbitals are perpendicular to neighboring $p_{x(y)}$ orbitals. Specifically, no hybridization takes place between these orbitals. In the band structure, we can see a triple energy degeneracy which is similar to a Dirac point, pierced by a third band. The triple band touching Dirac fermions was previously observed in other flat borophenes in experimental and theoretical studies.^{41,42}

In α' -4H borophene (right panel), hydrogenation pulls some of \textcircled{b} atoms, labeled with \textcircled{c} , out of the plane and forms a buckled structure. As a result, p_z orbitals of \textcircled{c} atoms would no longer be perpendicular to neighboring $p_{x(y)}$ orbitals, which leads to hybrid bonds. This hybridization can be seen very well in the PDOS and band structure. By hydrogenation, \textcircled{b} sites lose their dominance around the Fermi level. However, \textcircled{a} sites rather reserve their contribution, especially in the conduction band, because hydrogenation do not affect them directly. Subsequently, α' -4H borophene has dominated occupied \textcircled{c} - p_y states and unoccupied \textcircled{a} - p_z states in the valance and conduction band edges, respectively, which are separated with a relatively wide band gap.

These results are completely supported by the shapes of the wave functions at the VBM and CBM as represented in FIG. S2. At the VBM, the wave function is shaped like a dumbbell, which is distributed along the y -axis and centered on \textcircled{c} atoms, showing the contribution of \textcircled{c} - p_y orbitals. At the CBM, the dumbbell-shaped wave function has components along both x -axis and z -axis, showing the hybridization between \textcircled{c} - p_x and \textcircled{a} - p_z orbitals.

To highlight the role of buckling and orbital hybridization as a consequence, we also calculated the band structure for a conceptual model of flat α' -4H borophene. We re-optimized α' -4H borophene with a fixed z -component, to have the same buckling as α' borophene. The resulting band structure is available in FIG. S3 and shows no band gap. Therefore, we can conclude that the buckling induced by \textcircled{c} atoms is a strong cause for opening the band gap. It should be noted that the role of buckling in opening energy band gap has been widely considered in the community.⁴³⁻⁴⁵

The band gap calculated at the GGA-PBE level is 1.49 eV, which is underestimated by 1.0 eV compared to the experiment.¹⁰ Using the HSE03 and HSE06 hybrid functionals and considering a fraction of the exact exchange, the band gap is corrected to be 1.85 and 1.98 eV, respectively (see FIG. S4). Eventually, at the PBE0 level, the band gap is found to be 2.54 eV, in excellent agreement with the experimental band gap measured by UV-V spectrum (2.49 eV).

Although DFT gives adequate qualitative information about the electronic and optical properties, it does not account for the electron-electron and electron-hole interactions, which have a crucial role in 2D materials. Therefore, further investigations should be performed using many-body

perturbation calculations.

The QP band gap predicted by many-body GW theory is very sensitive to input parameters including the spin-orbit coupling (SOC), k -point sampling, vacuum space, number of virtual bands, energy cutoff, and self-consistent iteration. Therefore, it is mandatory to converge the band gap. We initially checked the effects of the SOC interaction. Due to small atomic mass of boron, except a slight downward shift in the electronic states, no noticeable spin splitting was found in the energy levels, and the band gap remained almost constant ($\Delta E_g \simeq 0.001$ eV). Hence, due to its excessive computational costs and negligible impacts, this interaction is excluded from the rest of the calculations.

Next, we performed a bunch of calculations to converge the QP band gap at the G_0W_0 level as a function of the (a) k -point sampling of Brillouin zone using 40 virtual bands and $L_z = 20$ Å; (b) vacuum space using 40 virtual bands and $5 \times 5 \times 1$ k -point mesh; and (c) the number of virtual bands using $L_z = 20$ Å and $5 \times 5 \times 1$ k -point mesh as illustrated in FIG. S6. We realized that a $9 \times 9 \times 1$ k -point mesh is enough for a satisfactory convergence within ~ 0.05 eV. Such a dense k -point mesh is also indispensable for an accurate description of the optical gap and binding energy. The vacuum space plays a crucial role in the determination of the QP band gap due to the long-range nature of screened Coulomb interaction. Generally, it is imposed to be between 20 to 30 Å. To ensure convergence within ~ 0.05 eV, we set the vacuum space to be 25 Å, which is the highest accuracy we could computationally afford. Our results also verified that at least 40 virtual bands are required for our many-body GW calculations. The corresponding band gap is essentially the same when 80 bands are included (see FIG. S6). Such rapid convergence concerning the number of unoccupied bands is mainly attributed to the absence of strongly localized states characterized by flat bands. Moreover, we tested the convergence of the QP band gap with respect to the number of iterations in partially self-consistent G_iW_0 and G_iW_i as shown in FIG. S6. Obviously, four iterations are sufficient to reach the convergence threshold of ~ 0.001 eV. Also, the energy cutoff for the exchange and correlation parts of the self-energy was set to be 50 and 10 Ry, respectively.

To ensure the accuracy of our many-body GW calculations, we calculated the QP band gaps of graphane (CH) and fluorographane (CF) monolayers. For example, for graphane, the band gap was predicted to be 5.62, 5.81, and 6.17 eV under the G_0W_0 , GW_0 , and GW levels of theory, respectively, which are in excellent agreement with 5.64, 5.89, and 6.28 eV reported in previous works.³¹ Also, the band gaps obtained for fluorographane agree very well with previous values as listed in Table S2.

After validation of the required accuracy, now we turn our attention to the GW results. The general shape of the QP band structure at the G_0W_0 level is similar to that obtained by the PBE functional, shown in FIG. S4. The VBM and CBM still locate at the same points. The Fermi level is still closer to the VBM, making α' -4H borophene a p-type semiconductor. The valence and conduction band edges are symmetrically dispersed, which indicates the presence of free

charge carriers. However, the inclusion of electron-electron interaction enlarges the band gap from 1.49 up to 1.98 eV. This value is larger than that of the HSE03 and exactly equal to that obtained by the HSE06. In other words, a similar accuracy could be achieved by the G_0W_0 as by the HSE06. At the GW_0 and GW levels, the QP band gap increases up to 2.23 and 2.52 eV, respectively, which is due to the presence of self-consistency. Overall, one can say that the GW level offers an accuracy similar to the PBE0 functional, in excellent agreement with the experiment.¹⁰ Also, the direct QP band gap at the Γ point are 3.09, 3.31, and 3.58 eV for G_0W_0 , GW_0 , and GW , respectively.

B. Optical properties

Excitonic effects play a crucial role in the optical properties of 2D materials for their weak dielectric screening. Hence, to have a reliable description of the optical properties, it is indispensable to take the electron-hole Coulomb interaction into account. In this section, we aim to present the excitonic optical spectra of α' -4H borophene achieved from solving the Bethe-Salpeter equation on top of various levels of the GW. To fully appreciate the many-body effects, we also calculated the optical spectra within random-phase approximation (RPA) on top of DFT and GW levels of theory, where the electron-hole interaction is neglected. FIG. 3 exhibits the imaginary part of the macroscopic dielectric function for light polarized along the x -direction at different levels, namely DFT+RPA, G_0W_0 +RPA, and G_0W_0 +BSE. As can be seen, the inclusion of electron-electron correlation completely reshapes the optical spectrum and leads to a significant blue shift (~ 1.4 eV), which is due to the self-energy correction. On the other hand, the electron-hole correlation results in a redshift (~ 0.92 eV) in the optical spectrum, owing to the cancellation effect between self-energy correction and excitonic effects. The electron-hole correlation also leads to an increase (decrease) of the oscillator strength of the first (second) peak. However, its main impact is the appearance of some bound excitons below the G_0W_0 direct band gap (3.09 eV) at the Γ point, which are missing in the G_0W_0 +RPA spectrum. As the imaginary part of the dielectric function is directly associated with the absorption spectrum, one can say that the excitonic effects increase the light absorption in the visible range (1.5 to 3.5 eV).

The DFT+RPA predicts the absorption edge to be ~ 1.48 eV, which is very close to the PBE band gap (1.49 eV). The first two peaks at G_0W_0 +RPA appear at 2.88 and 3.08 eV, respectively. They are near the G_0W_0 direct band gap (3.09 eV) at the Γ point, which is due to the exclusion of excitonic effects. Most importantly, the first peak at G_0W_0 +BSE (~ 1.96 eV) is found to lie between the PBE (1.49 eV) and G_0W_0 (1.98 eV) band gaps as it includes both the QP correction and excitonic effects. This peak (the so-called optical gap) originates from the direct transition (bright exciton) from the VBM to the conduction band, and corresponds to a strongly bound Frenkel exciton with a binding energy of $E_b \simeq 1.13$ eV. It is worth mentioning

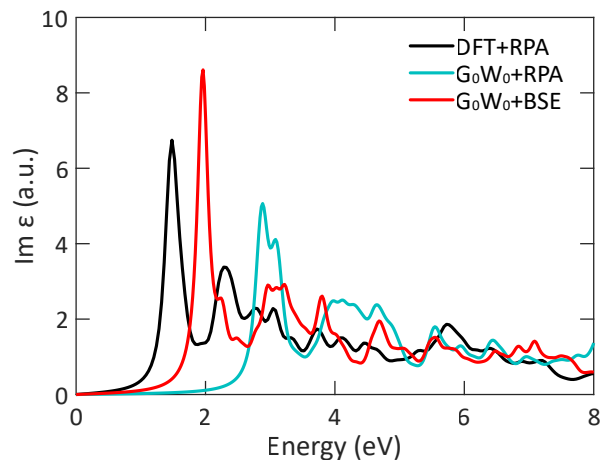


FIG. 3. The imaginary part of the dielectric function of α' -4H borophene for light polarized along the x -direction at different levels of theory: DFT+RPA (e-e and e-h correlations neglected), G_0W_0 +RPA (e-e correlation included and e-h correlation neglected), and G_0W_0 +BSE (both e-e and e-h correlations included).

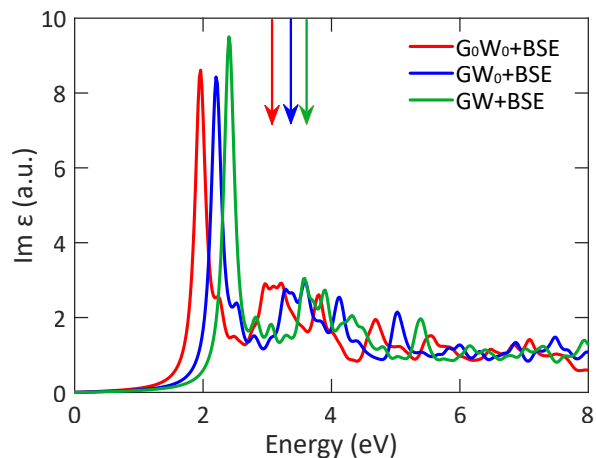


FIG. 4. The imaginary part of the dielectric function of α' -4H borophene including excitonic effects for light polarized along the x -direction under different degrees of self-consistency in the GW. Four iterations were used to obtain well-converged results from G_iW_0 and G_iW_i calculations. The QP (direct) band gaps are shown with arrows.

that the exciton binding energy is determined by the difference between the QP direct band gap and optical gap. The optical gap obtained from G_0W_0 +BSE is ~ 0.53 eV smaller than the experimental gap achieved from photoluminescence measurement (2.49 eV).¹⁰ This underestimation is attributed to the overscreening effects associated with building the susceptibility based on an underestimated Kohn-Sham band gap. Indeed, the small Kohn-Sham band gap leads to a spurious enhancement of the screening, and subsequently, to an underestimated optical gap.

For the considerable dependence of the G_0W_0 on the Kohn-Sham starting point and the exclusion of many-body exchange and correlation in the ground-state eigenvalues, we examined

the effects of self-consistency. FIG. 4 indicates the optical spectra of α' -4H borophene for light polarized along the x -direction under different degrees of self-consistency in the GW. As can be seen, iteratively updating the QP eigenvalues in the Green's function results in a blue shift (~ 0.24 eV) in the optical spectrum because it reduces the overestimation of the screening observed in the G_0W_0 . At this level of theory (i.e. GW_0+BSE), the shape of the spectrum is relatively preserved, and the optical gap is estimated to be ~ 2.20 eV with an exciton binding energy of $E_b \simeq 1.11$ eV. Therefore, one can say that E_b is independent of the self-consistency in Green's function. Moreover, the oscillator strength is only redistributed to higher energies with no considerable change.

Updating the screened Coulomb potential leads to a blue shift (~ 0.20 eV) as well, implying a larger self-energy correction in the GW compared to those in the G_0W_0 and GW_0 . The highest level of theory (i.e. $GW+BSE$) predicts the optical gap to be ~ 2.40 eV, which is slightly smaller than the GW band gap of ~ 2.52 eV. This value agrees very well with the experimental gap (2.49 eV)¹⁰ because $GW+BSE$ incorporates many-body effects in the ground state eigenvalues and meaningfully reduces the dependence on the DFT starting point using self-consistency. Here, the E_b is obtained ~ 1.18 eV, suggesting relatively stronger cancellation effects. Such a huge E_b is a signature of a strongly bound Frenkel exciton, showing ultrahigh stability of excitonic states against thermal dissociation, making α' -4H borophene a very promising candidate for exploring room-temperature optical applications. The final value is larger than those of phosphorene (0.86 eV), MoS_2 (0.96 eV), h-BN (0.80 eV), and many other semiconducting monolayers,⁴⁶⁻⁴⁹ turning α' -4H borophene into a highly competitive candidate. As the $GW+BSE$ gives the best results, the corresponding oscillator strength is shown in FIG. S7.

Because of the huge depolarization effect in 2D systems for the light polarization perpendicular to the surface ($E||z$),⁵⁰ we only focus on the optical spectra for light polarization parallel to the surface ($E||x, E||y$). As a consequence of the structural anisotropy in α' -4H borophene, a different optical spectrum is obtained for light polarized along the y -direction. As shown in FIG. S8, at all three levels of theory, the shape of the spectrum is different from that for light polarized along the x -direction (FIG. 4). Also, the first peak has weaker intensity. However, the same optical gap is achieved. Such in-plane optical anisotropy provides an additional degree of freedom for manufacturing optoelectronic devices.

It is worth mentioning that the QP band gap and exciton binding energy calculated at all three levels of theory (i.e. G_0W_0 , GW_0 , and GW) show an excellent agreement with the linear scaling law given as, $E_b = 0.21 E_g + 0.40$.⁵¹ The standard deviations are less than 0.05 eV, signifying well-converged results.

We also investigated the variation of band gap under biaxial tensile strain. As can be seen from FIG. S9, by increasing the tensile strain up to 10%, the QP and optical band gaps decrease linearly by ~ 0.4 and 0.7 eV, respectively. This is due to the reduction of buckling under tension. The exciton binding energy also experiences a decrease of ~ 0.3 eV, which

means the excitonic states are robust against tension up to 10%. It should be noted, in our previous work, we had presented the dynamical stability of α' -4H borophene under such tension by phonon dispersion, stress-strain, and energy-strain curves.²⁵

C. Bilayer α' -4H borophene

Observations of atomic force microscopy (AFM) have shown that the average thickness of a typical synthesized α' -4H borophene is about 0.78 nm,¹⁰ which is higher than the monolayer. To understand the effects of thickness on the electronic properties of α' -4H borophene, we studied the bilayer of this material. For this, we firstly measured the vertical distance between layers by means of variation of energy to thickness. As FIG. 5 (a) shows, the optimized thickness of a bilayer is achieved 0.785 nm, which is in great agreement with measurements of AFM. After gaining the interlayer distance, we re-optimized the structure with AA stacking. The electron difference density in FIG. 5 (a & b) shows that while a high electron extracting takes place by hydrogen atoms, the two layers do not trade much electrons within themselves, which implies the absence of strong covalent bonds and presence of weak van der Waals interactions. This might be due to the screening of H atoms among the boron layers. Because of the weak force between the layers, the lattice constant and bond lengths of the bilayer do not have a significant difference with the monolayer.

As shown in FIG. 5 (c), the AA-stacked bilayer α' -4H borophene is an indirect semiconductor with a band gap of 1.4 eV. Most 2D materials experience a topological band gap transition from their monolayer to bilayer or multilayer forms. For instance, from monolayer to bilayer, graphene opens a band gap of zero to 0.25 eV⁵² and, on the contrary, β antimonene closes its band gap from 0.76 eV to zero.⁵³ However, for the weak van der Waals interlayer interaction in bilayer α' -4H borophene, it experiences a very small gap change. The VBM is located at Γ point, and the CBM is within the Γ -K path. The bilayer α' -4H borophene is a p-type semiconductor because VBM is very close to the Fermi energy. This is due to electron deficiency in boron-based structures. In the VBM and CBM, the band structure dispersion is parabolic, which exhibits high mobility of electrons and holes. This inclines the high potential of α' -4H borophene in optoelectronic applications, even for thicknesses more than monolayer.

To see the impact of stacking mode on the electronic properties of bilayer, we slipped the upper layer along the lattice vector \mathbf{A}_1 as much as percentages of lattice constant, a. The energy difference between different stackings with respect to AA stacking is shown in FIG. 5 (d), which is less than 20 meV. These stackings can form Moiré patterns in borophene with no need to external strain or requirement of large superlattices. Our investigations show that stacking mode does not have significant impact on the band gap of borophene. The band gap remains indirect in all the stackings and, as shown in FIG. 5 (e), it fluctuate mildly around the

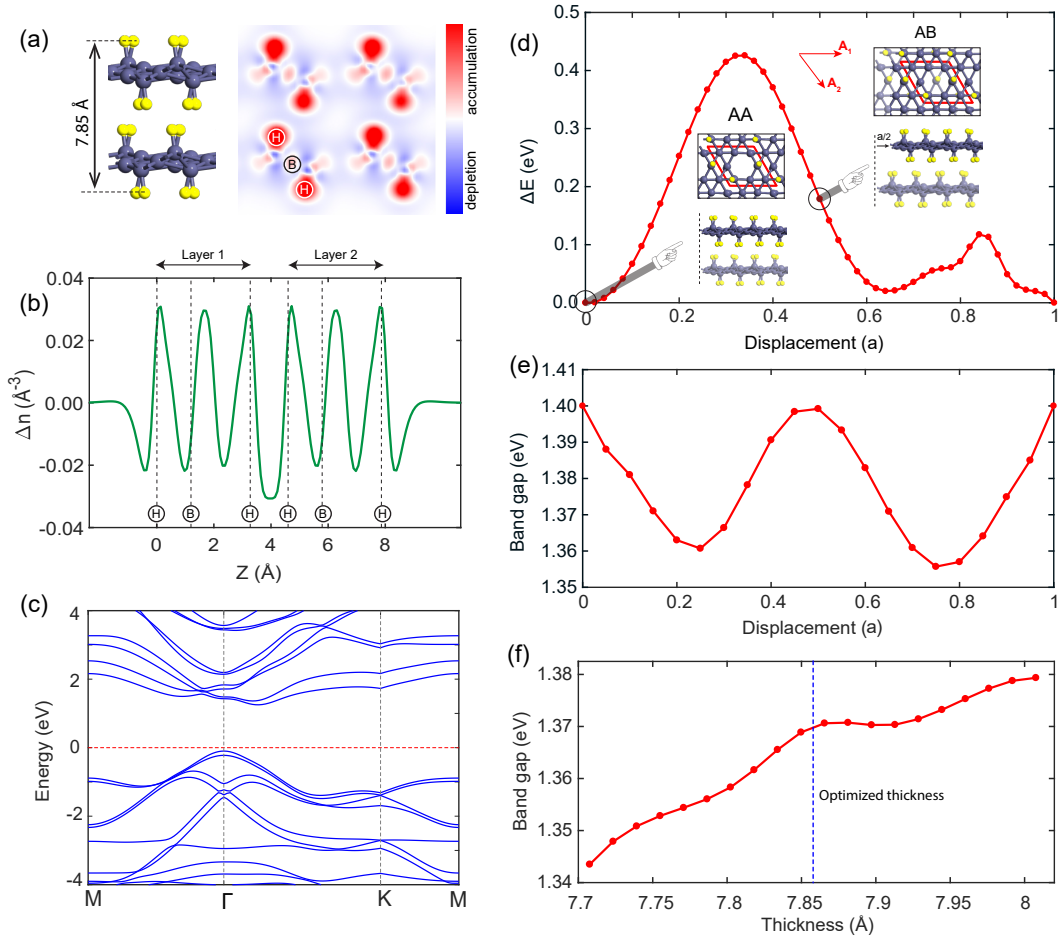


FIG. 5. Bilayer α' -4H borophene. (a) Side view and electron difference density map. (b) Variation of electron difference density with buckling. (c) Band structure of AA stacking. (d) Variation of bilayer energy with displacement of the upper layer with respect to AA stacking. (e) Variation of bilayer band gap with displacement of the upper layer. (f) Variation of band gap of AA stacking with thickness.

band gap of the AA stacking. When the displacement changes as half of the lattice constant (AB stacking), the band gap becomes equal to the band gap of the AA stacking. Because different stackings do not have very different band gaps, it is not possible to determine the stacking mode of bilayer α' -4H borophene through absorption spectrum.

To understand the dependence of electronic properties on the vertical distance between the layers, variation of band gap with interlayer distance is shown in FIG. 5 (f). Herein, with conserving the atomic arrangements, we tuned the interlayer distance to have thicknesses between 7.7 to 8 Å. We can see a mild increase of band gap with the increase of the thickness. In other words, a high increase in the distance cancels the weak van der Waals interaction between layers and renders the bilayer into two independent monolayers. On the contrary, decrease of vertical interlayer distance increases the interactions and leads to a mild decrease in the band gap. Our investigations show that interlayer distance does not have any impact on the nature of indirect band gap of α' -4H borophene. It can be concluded that for the weak van der Waals interaction between the layers and existence

of light weight atoms, vertical pressure and slipping of the layers do not make significant change in optical properties of the structure, therefore, no gap difference was observed for different thickness of the structure in experiment.¹⁰

V. CONCLUSION

In summary, we reported the electronic and excitonic optical properties of α' -4H borophene using first-principles many-body calculations. We firstly tracked the mechanism in which the metallic α' borophene turns into the semiconducting α' -4H borophene. It was found that hydrogenation increases the buckling height and breaks the mirror symmetry of α' borophene, which results in hybridization between p_z and neighboring $p_{x(y)}$ orbitals and opens a wide band gap in α' -4H borophene. Then, we calculated the quasiparticle band gap to be 1.98, 2.23, and 2.52 eV at the G_0W_0 , GW_0 , and GW levels of theory, respectively. In the following, we solved the Bethe-Salpeter equation on top of the GW. The optical spectrum at GW+BSE

shows that the direct optical excitation is characterized by an optical band gap of ~ 2.40 eV, which is in excellent agreement with the experiment (2.49 eV). The exciton binding energy was calculated to be ~ 1.18 eV, which is a signature of a strongly bound Frenkel exciton, suggesting ultrahigh stability of excitonic states against thermal dissociation. We also investigated the bilayer α' -4H borophenes with different stackings and thicknesses. It was found that they have similar electronic properties to the monolayer, which gives them similar potentials. These features together with great air-stability and mechanical strength suggest α' -4H borophene as a desirable material for flexible optoelectronic applications at

room temperature.

ACKNOWLEDGMENT

We are thankful to the Research Council of the University of Guilan for the partial support of this research.

DECLARATION OF INTERESTS

The authors declare that they have no conflict of interest.

* m.bagheri@guilan.ac.ir

- ¹ A. J. Mannix, Z. Zhang, N. P. Guisinger, B. I. Yakobson, and M. C. Hersam, *Nat. Nanotechnol.* **13**, 444 (2018).
- ² L. Liu, Z. Zhang, X. Liu, X. Xuan, B. I. Yakobson, M. C. Hersam, and W. Guo, *Nano Lett.* **20**, 1315 (2020).
- ³ E. S. Penev, A. Kutana, and B. I. Yakobson, *Nano Lett.* **16**, 2522 (2016).
- ⁴ S. I. Vishkayi and M. B. Tagani, *Phys. Chem. Chem. Phys.* **19**, 21461 (2017).
- ⁵ R. A. Vajary, M. B. Tagani, and S. I. Vishkayi, *Mod. Phys. Lett. B* **32**, 1850347 (2018).
- ⁶ S. I. Vishkayi and M. B. Tagani, *Phys. Chem. Chem. Phys.* **20**, 10493 (2018).
- ⁷ A. J. Mannix, X.-F. Zhou, B. Kiraly, J. D. Wood, D. Alducin, B. D. Myers, X. Liu, B. L. Fisher, U. Santiago, and J. R. Guest, *Science* **350**, 1513 (2015).
- ⁸ S. Arabha, A. H. Akbarzadeh, and A. Rajabpour, *Compos. B. Eng.* **200**, 108260 (2020).
- ⁹ D. Ayodhya and G. Veerabhadram, *FlatChem* **19**, 100150 (2020).
- ¹⁰ C. Hou, G. Tai, J. Hao, L. Sheng, B. Liu, and Z. Wu, *Angew. Chem.* (2020).
- ¹¹ Z. Xie, X. Meng, X. Li, W. Liang, W. Huang, K. Chen, J. Chen, C. Xing, M. Qiu, B. Zhang, G. Nie, N. Xie, X. Yan, and H. Zhang, *Research* **2020**, 2624617 (2020).
- ¹² C. D. Entwistle and T. B. Marder, *Angew. Chem. Int. Ed.* **41**, 2927 (2002).
- ¹³ L. Kong, L. Liu, L. Chen, Q. Zhong, P. Cheng, H. Li, Z. Zhang, and K. Wu, *Nanoscale* **11**, 15605 (2019).
- ¹⁴ N. Powar and R. Pandav, *J. Chem. Rev.* **1**, 271 (2019).
- ¹⁵ G. Bhattacharyya, A. Mahata, I. Choudhuri, and B. Pathak, *J. Phys. D: Appl. Phys.* **50**, 405103 (2017).
- ¹⁶ S. Suehara, T. Aizawa, and T. Sasaki, *Phys. Rev. B* **81**, 085423 (2010).
- ¹⁷ R. Wu, I. K. Drozdov, S. Eltinge, P. Zahl, S. Ismail-Beigi, I. Božović, and A. Gozar, *Nat. Nanotechnol.* **14**, 44 (2019).
- ¹⁸ B. Kiraly, X. Liu, L. Wang, Z. Zhang, A. J. Mannix, B. L. Fisher, B. I. Yakobson, M. C. Hersam, and N. P. Guisinger, *ACS Nano* **13**, 3816 (2019).
- ¹⁹ Q. Zhong, L. Kong, J. Gou, W. Li, S. Sheng, S. Yang, P. Cheng, H. Li, K. Wu, and L. Chen, *Phys. Rev. Mater.* **1**, 021001 (2017).
- ²⁰ H. Liu, J. Gao, and J. Zhao, *Sci. Rep.* **3**, 1 (2013).
- ²¹ C. R. Ryder, J. D. Wood, S. A. Wells, Y. Yang, D. Jariwala, T. J. Marks, G. C. Schatz, and M. C. Hersam, *Nat. Chem.* **8**, 597 (2016).
- ²² J. E. Johns and M. C. Hersam, *Acc. Chem. Res.* **46**, 77 (2013).
- ²³ Q. Li, V. S. C. Kolluru, M. S. Rahn, E. Schwenker, S. Li, R. G. Hennig, P. Darancet, M. K. Y. Chan, and M. C. Hersam, *Science* **371**, 1143 (2021).
- ²⁴ M. A. Mohebpour, S. M. Mozvashi, S. I. Vishkayi, and M. B. Tagani, *Sci. Rep.* **10**, 1 (2020).
- ²⁵ S. M. Mozvashi, M. A. Mohebpour, S. I. Vishkayi, and M. B. Tagani, *Sci. Rep.* **11**, 1 (2021).
- ²⁶ P. Cudazzo, C. Attaccalite, I. V. Tokatly, and A. Rubio, *Phys. Rev. Lett.* **104**, 226804 (2010).
- ²⁷ L. Yang, J. Deslippe, C.-H. Park, M. L. Cohen, and S. G. Louie, *Phys. Rev. Lett.* **103**, 186802 (2009).
- ²⁸ M. Shishkin and G. Kresse, *Phys. Rev. B* **75**, 235102 (2007).
- ²⁹ M. S. Hybertsen and S. G. Louie, *Phys. Rev. B* **34**, 5390 (1986).
- ³⁰ C. Liu, J. Kloppenburg, Y. Yao, X. Ren, H. Appel, Y. Kanai, and V. Blum, *J. Chem. Phys.* **152**, 044105 (2020).
- ³¹ F. Karllicky and M. Otyepka, *J. Chem. Theory Comput.* **9**, 4155 (2013).
- ³² M. Shahrokhi and C. Leonard, *J. Alloys Compd.* **682**, 254 (2016).
- ³³ M. Shishkin and G. Kresse, *Phys. Rev. B* **74**, 035101 (2006).
- ³⁴ X. Blase, I. Duchemin, D. Jacquemin, and P.-F. Loos, *J. Phys. Chem. Lett.* **11**, 7371 (2020).
- ³⁵ M. Gajdoš, K. Hummer, G. Kresse, J. Furthmüller, and F. Bechstedt, *Phys. Rev. B* **73**, 045112 (2006).
- ³⁶ M. Shahrokhi and C. Leonard, *J. Alloys Compd.* **693**, 1185 (2017).
- ³⁷ M. Rohlffing and S. G. Louie, *Phys. Rev. Lett.* **80**, 3320 (1998).
- ³⁸ M. Rohlffing and S. G. Louie, *Phys. Rev. B* **62**, 4927 (2000).
- ³⁹ P. Giannozzi, S. Baroni, N. Bonini, M. Calandra, R. Car, C. Cavazzoni, D. Ceresoli, G. L. Chiarotti, M. Cococcioni, and I. Dabo, *J. Phys.: Condens. Matter* **21**, 395502 (2009).
- ⁴⁰ A. A. Mostofi, J. R. Yates, G. Pizzi, Y.-S. Lee, I. Souza, D. Vanderbilt, and N. Marzari, *Comput. Phys. Commun.* **185**, 2309 (2014).
- ⁴¹ M. Ezawa, *Phys. Rev. B* **96**, 035425 (2017).
- ⁴² B. Feng, O. Sugino, R.-Y. Liu, J. Zhang, R. Yukawa, M. Kawamura, T. Iimori, H. Kim, Y. Hasegawa, and H. Li, *Phys. Rev. Lett.* **118**, 096401 (2017).
- ⁴³ S. K. Radha and W. R. L. Lambrecht, *Phys. Rev. B* **101**, 235111 (2020).
- ⁴⁴ Y. Umeno, M. Sato, M. Sato, and H. Shima, *Phys. Rev. B* **100**, 155116 (2019).
- ⁴⁵ A. Nijamudheen, R. Bhattacharjee, S. Choudhury, and A. Datta, *J. Phys. Chem. C* **119**, 3802 (2015).
- ⁴⁶ D. Y. Qiu, H. Felipe, and S. G. Louie, *Phys. Rev. Lett.* **111**, 216805 (2013).

- ⁴⁷ M. Kolos and F. Karlický, *Phys. Chem. Chem. Phys.* **21**, 3999 (2019).
- ⁴⁸ L. Xu, M. Yang, S. J. Wang, and Y. P. Feng, *Phys. Rev. B* **95**, 235434 (2017).
- ⁴⁹ V. Tran, R. Soklaski, Y. Liang, and L. Yang, *Phys. Rev. B* **89**, 235319 (2014).
- ⁵⁰ L. Yang, C. D. Spataru, S. G. Louie, and M.-Y. Chou, *Phys. Rev. B* **75**, 201304 (2007).
- ⁵¹ J.-H. Choi, P. Cui, H. Lan, and Z. Zhang, *Phys. Rev. Lett.* **115**, 066403 (2015).
- ⁵² Y. Zhang, T.-T. Tang, C. Girit, Z. Hao, M. C. Martin, A. Zettl, M. F. Crommie, Y. R. Shen, and F. Wang, *Nature* **459**, 820 (2009).
- ⁵³ G. Wang, R. Pandey, and S. P. Karna, *ACS Appl. Mater. Interfaces* **7**, 11490 (2015).